Acta Materialia 151 (2018) 443–453

Contents lists available at ScienceDirect

Acta Materialia

journal homepage: www.elsevier.com/locate/actamat

Full length article

A geometric model for the fracture toughness of porous materials

H. Jelitto*, G.A. Schneider

Institute of Advanced Ceramics, Hamburg University of Technology, 21073 Hamburg, Germany

ARTICLE INFO

Article history:
Received 24 November 2017
Received in revised form
27 February 2018
Accepted 12 March 2018
Available online 16 March 2018

Keywords:
Fracture toughness
Toughness
Elastic properties
Porosity
Modeling

ABSTRACT

Different models for the fracture toughness, K_{IC}, of porous materials have been proposed to describe K_{IC} as a function of the porosity P. They have in common that beside P at least one additional parameter exists that has to be adjusted to the measured data. Based on the cubic structure, we present a geometrical 3D model without any arbitrary parameter, which predicts the K_{IC}, the toughness, G_C, and the Young's modulus, E, of a porous material. The model comprises three variants, depending on the material properties like open or closed porosity. It is in good agreement with a large amount of experimental data from different research groups.

1. Introduction

If the fracture toughness of a dense material, K_{IC}, is known, it is desirable to predict the fracture toughness of the same material, having the porosity P. This applies for example to ceramics with low porosity as also to polymer foams and sponges. The requirement for our model and most other models in the literature is that the material is isotropic and behaves linear-elastically, when it is loaded until fracture.

One existing and widely used model was developed by Ashby, Maiti, and Gibson [1–3]. They solved the problem on a microscopic (cell) level. For open porosity, they got the following equation:

$$K_{IC}^{*} = c_1 \sigma_f \sqrt{\pi w} \left(\frac{\rho}{\rho_s}\right)^{3/2} = c_1 \sigma_f \sqrt{\pi w}\,(1-P)^{3/2} \quad (1)$$

Here, K_{IC}^{*} is the fracture toughness of the porous material, c_1 a normalization factor, σ_f the fracture strength of the dense material, w the size of the cells, ρ the density of the porous material, and ρ_s the density of the dense material. In addition, K_{IC}^{*} is given in an alternative way with regard to $\rho/\rho_s = 1 - P$. In their calculation for open porosity, the authors used the relation $\rho/\rho_s \propto t^2/w^2$, in which t is the thickness of the ligaments between two pores (cells). However, this relation is valid only for $t << w$, which implies that the porosity has to be relatively high. Consequently, Maiti et al. applied their model to rigid polymer foams with porosities of 68%–97%, and obtained a good agreement. In order to get such an agreement, they had to adjust their model to the measured data with the normalization factor $c_1 = 0.65$. As Maiti et al. stated, Eq. (1) shows a slight dependence of K_{IC}^{*} on the size w of the cells. The characteristic of the fracture toughness according to $(\rho/\rho_s)^{3/2}$ was used, for example, also in Refs. [4–6]. For closed porosity, Maiti et al. derived an equation like Eq. (1) with the exponent 2 instead of 3/2 and a normalization factor c_2, which was not further specified [2].

Other authors worked on a more general approach, like for example $K_{IC}^{*} \propto (\rho/\rho_s)^n$, where the exponent n was adapted to the experimental data [7–10]. Yang et al. [11], for instance, provided an equation for the relative fracture toughness:

$$\frac{K_{IC}^{*}}{K_{IC}} = \left(1 - \alpha P - \beta P^2\right) \quad (2)$$

with the parameters α and β being adjusted, correspondingly. Also finite element calculations were done to predict the dependence between K_{IC}^{*} and P [10,12]. It seems that all of the approaches in the literature have more or less empirical character, since in any case at least one parameter has to be fitted to the experimental data. Such parameters do not have a physical meaning. (Detailed information about cellular ceramics is given, for example, in the books of Gibson/Ashby [3], Rice [13], Scheffler/Colombo, Eds., [14], and also in Ashby/Bréchet [15].) In contrast, we present an analytical, geometrical 3D model on the basis of the cubic structure which

* Corresponding author.
E-mail address: h.jelitto@tuhh.de (H. Jelitto).

https://doi.org/10.1016/j.actamat.2018.03.018

does not include any arbitrary parameter.

2. The geometric model

The approach is based on the concept of the toughness

$$G_C = \frac{K_{IC}^2}{E} \tag{3}$$

which is the energy release during crack advance per crack face area (plane stress). E is the elastic modulus. In the following, G_C^* and G_C are the toughness of the porous and the dense material. The main idea is that the normalized or "relative" toughness, G_C^*/G_C, is given by the ratio of the substantial crack surface to the total crack surface. The latter one includes empty spaces like pores and cracks etc. This approach was already applied by Maiti et al. [2]. However, they assumed high porosity, while our ansatz is valid for any porosity. Here, "relative" or "normalized" always means "in relation to the dense material." The model is subdivided into three variants A–C, described in the following. To simplify matters, they are also named "model A" to "model C", although they represent together one model.

2.1. Model A – closed porosity

For closed porosity, the pores are idealized as cubes and arranged as in Fig. 1a). The size of the unit cell (lattice constant) is w, and the material walls between the cubic pores have the thickness t. Now, we fracture the material in the plane of minimum fracture surface, which is, e.g., the 100-plane. The corresponding (idealized) crack face is shown in Fig. 1b). In a real porous material, the crack face is not totally planar but grows along the path with the nearest and largest pores. In our simple cubic structure, this would mean fracture along the 100-plane with the lowest energy release.

We define the dimensionless number $d = t/w$ with $0 < d \leq 1$. Thus, on the basis of Fig. 1a) we obtain for the porosity:

$$P = \frac{(w-t)^3}{w^3} = (1-d)^3 \tag{4}$$

and it follows

$$d = 1 - P^{1/3} \tag{5}$$

If we calculate the relative amount of substantial crack face area (of the fractured cell walls) from Fig. 1b), we get

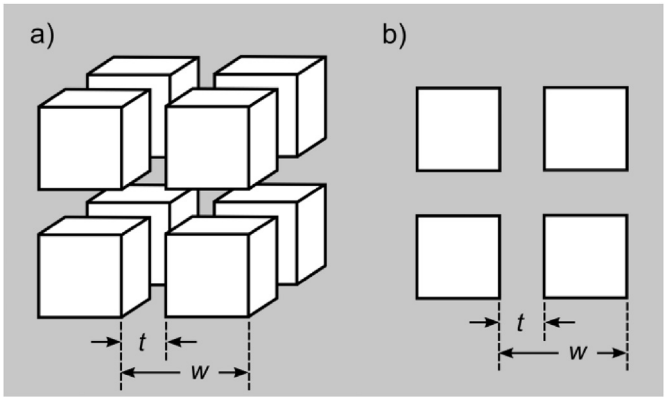

Fig. 1. a) Closed porosity with the pores idealized in a cubic arrangement, b) fracture surface with (quadratic) pores.

$$\frac{G_C^*}{G_C} = \frac{w^2 - (w-t)^2}{w^2} = 1 - (1-d)^2 \tag{6}$$

The replacement of d according to Eq. (5) yields for closed porosity:

$$\frac{G_C^*}{G_C}(\text{mod. A}) = 1 - P^{2/3} \tag{7}$$

2.2. Model B – open porosity

For open porosity, the material is once more idealized by a simple cubic structure as given in Fig. 2a). The lattice constant and the thickness of the ligaments are again w and t.

At first, we calculate the porosity as a function of d. With the volume of the unit cell being w^3, we find with regard to Fig. 2a):

$$P = \frac{w^3 - t^3 - 3t^2(w-t)}{w^3} = 2d^3 - 3d^2 + 1 \tag{8}$$

By considering Fig. 2b), we simply obtain the relative toughness

$$\frac{G_C^*}{G_C} = \frac{t^2}{w^2} = d^2 \tag{9}$$

In order to get the relative toughness as a function of P, we have to replace d in Eq. (9) by P, and hence to solve equation (8) for d. The computing software *Maple* [16] provides the solution:

$$d = \frac{1}{2}\cdot\left(-1 + 2P + 2\sqrt{P^2 - P}\right)^{1/3} + \frac{1}{2\left(-1 + 2P + 2\sqrt{P^2 - P}\right)^{1/3}} + \frac{1}{2} \tag{10}$$

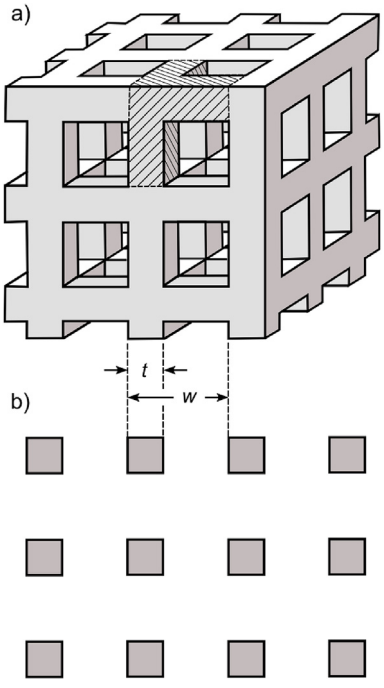

Fig. 2. a) Scheme of cubic structure with open porosity. The shaded part represents the material of one unit cell. b) Cross section and crack face, respectively, along the 100-plane.

Because of $0 \le P < 1$, the term under the square root is negative (except for $P = 0$), and therefore, both expressions in brackets are not real but complex. Furthermore, the second and third roots cause some ambiguities, in which most of the cases are not the result we need. Nevertheless, it is possible to find an analytical solution for the physically relevant part, as shown in the Appendix A. Introducing the solution, based on Eq. (A4) in the Appendix, into Eq. (9) gives the result for open porosity:

$$\frac{G_C^*}{G_C}(\text{mod. B}) = \left[\cos\left(\frac{2\pi - \cos^{-1}(2P-1)}{3} \right) + \frac{1}{2} \right]^2 \qquad (11)$$

An easy way to check the validity of this equation exists independently of Eq. (10). What we need is the toughness and the porosity together in one diagram. With the equations (8) and (9), we have both quantities as a function of d. So, we can use these two equations as a parametric representation $P(d)$ and $(G_C^*/G_C)(d)$. The outcome verifies the result of Eq. (11).

2.3. Model C – open porosity with disconnections

If the porosity becomes high and approaches 100%, the ligaments in Fig. 2 become very thin. In many brittle materials like ceramics, such filigree beams are unrealistic. So, with increasing porosity it is likely that more and more filaments are disconnected, e.g., during the sintering process (see Fig. 3).

With regard to Figs. 2 and 3, let us name the relative amount of disconnected ligaments X. Then two extreme cases seem reasonable. For the porosity being zero, the amount X also vanishes. If the porosity becomes almost 1, also X approaches 1. Now, the simplest assumption is that X is a linear function of the porosity, P, implying that X and P are not only proportional but identical. The relative amount of *existing* ligaments is $1-X = 1-P$. Therefore, the expression for the toughness in Eq. (11) would get an additional factor $(1-P)$. However, the comparison with experimental data reveals that, for a certain porosity, the extent of disconnections is not always the same for different materials. Therefore, we add an exponent $n > 0$, which yields quantitative information about the amount of disconnections. This creates the portion of existing ligaments $Y(P) = (1-P)^n$, which is the simplest modification that satisfies the boundary conditions $Y(0) = 1$ and $Y(1) = 0$ for positive n. Adding this factor and replacing P by Eq. (8) yields:

$$\frac{G_C^*}{G_C} = d^2 \cdot (1-P)^n = d^2 \cdot \left(-2d^3 + 3d^2 \right)^n \qquad (12)$$

As a function of P, we get explicitly:

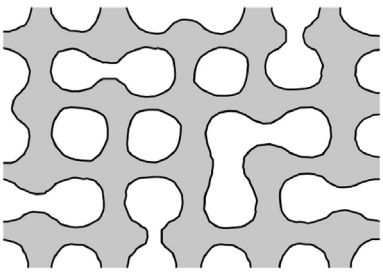

Fig. 3. Schematic cross section through the ligaments in a cell structure, similar to that one in Fig. 2, with disconnections. The relative amount of disconnections in this figure is approximately 20%. The disconnections exist also in the third dimension, which is not shown here.

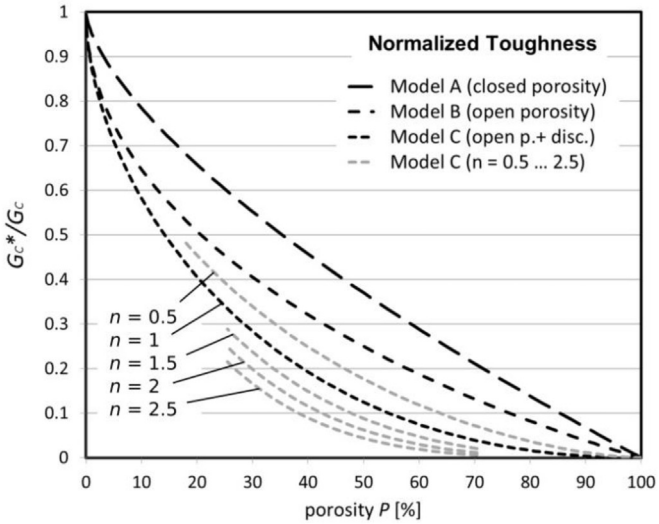

Fig. 4. Relative toughness as a function of the porosity P with different parameters n of the model C.

$$\frac{G_C^*}{G_C}(\text{mod. C}) = \left[\cos\left(\frac{2\pi - \cos^{-1}(2P-1)}{3} \right) + \frac{1}{2} \right]^2 \cdot (1-P)^n \qquad (13)$$

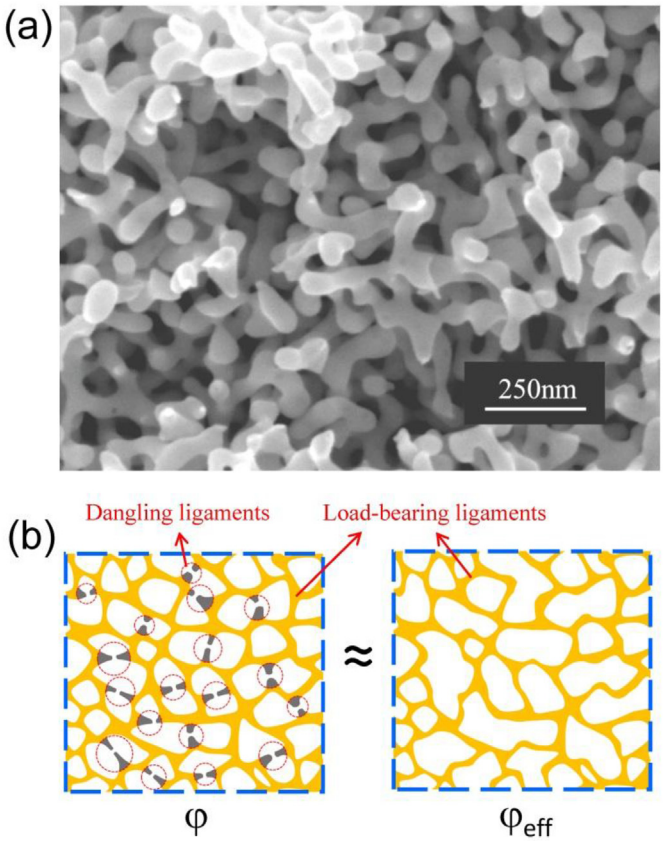

Fig. 5. a) SEM image of nanoporous (np) gold with ligament diameter of (43 ± 5) nm [17]. b) Schematic illustration of np structure with broken or dangling ligaments, and a mechanically equivalent structure that is obtained by removing dangling ligaments. Here, φ means relative density and φ_{eff} is defined as the effective relative density [17]. (For the colour version of this figure, the reader is referred to the Web version of this article.)

The exponent n is directly correlated with the amount of disconnected ligaments. The higher this exponent becomes, the larger is the latter amount, meaning that this parameter is not arbitrary. The simplest case of $n = 1$ in Eq. (13) can be seen as the basic form of model variant C. The limiting case $n = 0$ is identical to variant B. As in model B, Eqs. (8) and (12) can be used for an equivalent parametric representation. Fig. 4 represents the three model variants A–C, where variant C is given with a few alternative exponents n.

There might be some concern, whether the main idea of model C is an arbitrary assumption. In their recent research, Liu et al. used just this ansatz to explain the anomalously low strength and stiffness of nanoporous gold. In Fig. 5b), taken from their publication [17], the disconnections in the material are named “broken or dangling ligaments.” Furthermore, this effect is also experimentally observed (Fig. 5a). Of course, this does not mean that all materials behave like this, but at least for some of them this seems to be a realistic picture. So, the paper of Liu et al. confirms very well the basic idea of variant C.

2.4. Normalized Young's modulus

The publications of experimental data concerning porous materials provide mainly the fracture toughness, K_{IC}, and not the toughness, G_C. So, in order to compare our model with experimental results, we have to convert the toughness, G_C, accordingly. Due to Eq. (3), we need to determine the elastic modulus, E^*, of the porous material in order to obtain K^*_{IC}. This will be done on the same geometrical basis by assuming the cubic structures like in the Figs. 1–3 and by loading the structure vertically and perpendicularly to the principal horizontal plane.

Prior to the calculation, a question arises concerning the isotropy of the elastic modulus within our model. Anisotropy might exist if the loading of the ligaments changes from tension or compression to bending, depending on the loading direction. The following arguments suggest that, in our model, E^* is almost independent from the loading direction: 1. The quadratic walls of closed cells act as if diagonal struts exist in the walls. Therefore, the structure behaves like a triangular framework, which is very stiff with E^* being almost isotropic. 2. For open porosity, bending is possible mainly for thin ligaments, which means high porosity. For medium and low porosity, bending is negligibly low. 3. If the process zone at the crack tip is small compared to the length of the crack front, we have plane strain condition in the middle part of the crack front. This means that transverse strain is not possible. Even if the square structure is loaded diagonally, the ligaments are loaded mainly in compression or tension but not in bending. So, we assume that the following estimate of the Young's modulus is more or less valid for any loading direction.

On the basis of Figs. 1 and 2, we apply the rule of mixture two times in each case, first for a parallel and secondly for a serial arrangement. These basic calculations with a slight modification are summarized in Appendix B and yield the following normalized Young's moduli for the models A–C:

$$\frac{E^*}{E}(\text{mod. A}) = \left(\frac{1-d}{-d^2+2d} + \frac{1}{-d+2+(1-d)^2 d^{-1/2}}\right)^{-1} \tag{14}$$

$$\frac{E^*}{E}(\text{mod. B}) = \frac{-2d^3+3d^2}{2d^2-4d+3} \tag{15}$$

$$\frac{E^*}{E}(\text{mod. C}) = \frac{-2d^3+3d^2}{2d^2-4d+3}\cdot(1-P)^n = \frac{\left(-2d^3+3d^2\right)^{n+1}}{2d^2-4d+3} \tag{16}$$

For model A, $d(P)$ is given by Eq. (5) and for the models B and C by:

$$d = \cos\left(\frac{2\pi - \cos^{-1}(2P-1)}{3}\right) + \frac{1}{2} \tag{17}$$

which follows from Eq. (A4). Of course, with increasing parameter n, in average the remaining ligaments become longer, and therefore, bending effects might become more important. Such bending or buckling is not considered in the model so that the real Young's modulus decreases even more. Nevertheless, we expect a monotonic decrease of E^* with respect to n, and thus, n can be seen as a parameter, characterizing well the microscopic structure according to the average length of the ligaments. More information is provided in the comparison of experiments and model (chapter 4).

2.5. Normalized fracture toughness

On the basis of Eq. (3) and with E being the Young's modulus of the solid material, the normalized fracture toughness is:

$$\frac{K^*_{IC}}{K_{IC}} = \sqrt{\frac{G^*_C\, E^*}{G_C\, E}} \tag{18}$$

Note that Eq. (18) is exactly valid for the state of plane stress and almost exactly valid for plane strain. If the Poisson ratios (ν) for the porous and the dense material are more or less identical, the two factors ($1-\nu^2$) in the case of plain strain cancel each other. For model variant A, we have to replace G^*_C/G_C and E^*/E by means of Eqs. (7) and (14). With $d = 1 - P^{1/3}$, we obtain

$$\frac{K^*_{IC}}{K_{IC}}(\text{mod. A}) = \left(1-P^{2/3}\right)^{1/2} \cdot\left(\frac{1-d}{-d^2+2d} + \frac{1}{-d+2+(1-d)^2 d^{-1/2}}\right)^{-1/2} \tag{19}$$

(If replacing P by Eq. (4), the right side of Eq. (19) is dependent only on d.) Further modification of Eq. (19) does not simplify the result. Therefore, we leave the equation as it is. For the following variants B and C, d is given by Eq. (17). In case of model variant B, we replace again the right side of Eq. (18) by means of Eqs. (9) and (15), which leads to:

$$\frac{K^*_{IC}}{K_{IC}}(\text{mod. B}) = d^2\cdot\left(\frac{-2d+3}{2d^2-4d+3}\right)^{1/2} \tag{20}$$

Finally, model C with Eqs. (12) and (16) and replacing P by Eq. (8) yields:

$$\frac{K^*_{IC}}{K_{IC}}(\text{mod. C}) = d^2\cdot\left(\frac{-2d+3}{2d^2-4d+3}\right)^{1/2}\cdot(1-P)^n = \frac{d\cdot\left(-2d^3+3d^2\right)^{n+1/2}}{\left(2d^2-4d+3\right)^{1/2}} \tag{21}$$

In summary, each of the three model variants yields the normalized quantities of the toughness G^*_C, the fracture toughness K^*_{IC}, and the Young's modulus E^*. In each case and for each model A

to C, an equation exists which is solely dependent on d. So, together with the corresponding functions $P(d)$ of Eqs. (4) and (8), a parametric representation can always be realized alternatively. In model A, $d(P)$ is generally given by Eq. (5) and in the models B and C by Eq. (17), implying that all of the quantities can be expressed as a function of P, too. The exponent n in Eq. (21) is correlated again with the amount of disconnected ligaments. Other aspects and the limits of this model will be examined in chapter 4.

3. Measurements of porous materials

For the comparison, the experimental data of twelve different research groups, who tested porous materials, are considered and briefly described. Flinn et al. [8] used data from tests of alumina, measured by Knechtel [9], and provided directly the relative fracture toughness. Deng et al. [18] measured pure alumina, too (label A), and also two mixtures with aluminum hydroxide (labels AH60 and AH90). They presented only the absolute fracture toughness without giving the value for the dense material. Anyway, for pure alumina it was easy to extrapolate the K_{IC} from 97% density to 100% (see Table 1 and Fig. 6). For the mixture of Al_2O_3 and $Al(OH)_3$, the maximum density was about 89%, and so, the extrapolation would be less certain. However, the authors state that in this case and for lower porosities the addition of $Al(OH)_3$ does not improve the K_{IC}. Furthermore, the trends of the data for pure alumina and the mixture were almost identical so that we use the same 100%-value for the mixed material AH60. The fracture toughness data of the material AH90 are not included here, because a reliable extrapolation to the dense material was not possible. Yang et al. [11] and also Ohji [19] tested porous silicon nitride (α-Si_3N_4 with 5 wt% Yb_2O_3) and provided directly the relative densities. Hong et al. [20] used two variants of TiB_2, where the powder was cold isostatically pressed at 10 and 50 MPa. The measured densities between 45% and 95% allow for an easy extrapolation to 100%. Samborski and Sadowski [21] worked with porous alumina and magnesia with densities up to 96.5% and 91.5%, respectively, at static and also dynamic, periodic loading. Only the static measurements and only the alumina results are used, because for the magnesia tests the extrapolation to the full density includes higher uncertainty. Goushegir et al. [22] performed tests with alumina fibers in a RBAO matrix (reaction bonded aluminum oxide) of different porosities. Also here, the extrapolation of the fracture toughness for the dense material could be done easily. For the graphical extraction of the experimental data, the published diagrams were magnified – if necessary – and then provided with a precise grid before determining accurately the measured quantities.

For further information and in order to get an impression about the reliability of the results, the experimental details and the extracted numerical data from each research group, used in this paper, are summarized in a separate reference in “Data in Brief” [23].

Maiti, Ashby, and Gibson [2], who presented the model of Eq. (1), did not test ceramics but foamed polymethacrylimid (PMI-E), a hard polymer with a very high porosity. The relative fracture toughness was presented in a double logarithmic plot. Within their plot, they included also some data from McIntyre/Anderton [24] as well as from Fowlkes [25], who tested polyurethane foams (PUR). The whole data were used here and taken from the magnified diagram (Fig. 3 in Ref. [2]) by creating an equidistant grid, extracting graphically the logarithmic data, and then transforming them from the logarithmic to the linear scale. In this case, an additional check was performed: The numerical data were plotted again in a double logarithmic diagram and compared with the original plot. The diagrams looked identical.

Table 1
Estimated fracture toughness for the dense material, extrapolated from the experimental data given in the references.

Material	Reference	K_{IC} [MPa$\sqrt{m}$]
Al_2O_3–A, Al_2O_3–AH60	Fig. 8a) in Ref. [18]	5.44
TiB_2 (10/50 MPa)	Fig. 5 in Ref. [20]	3.21/4.18
Al_2O_3	Fig. 5 in Ref. [21]	3.63
Al_2O_3-fibers + RBAO-matrix	Fig. 3 in Ref. [22]	4.16

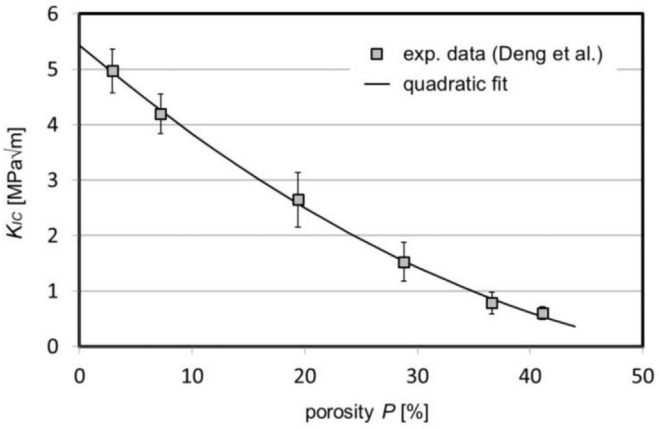

Fig. 6. Quadratic fit to the experimental data of the material Al_2O_3-A [18]. With the nonlinear extrapolation to zero porosity, the fracture toughness of the dense material is estimated (5.44 MPa$\sqrt{m}$).

The extrapolation, to get the fracture toughness of the dense material, was done by fitting a quadratic function to the measured data and then using the function value at zero porosity. Afterwards, the fracture toughness of the porous substances could be normalized by division through the extrapolated data. Concerning K_{IC}, this was necessary for four references. The estimated values of these references are listed in Table 1 so that they can be checked by the reader. The error of this extrapolation should be in the range of a few percent, like for instance 5%. An example for the data of Deng et al. [18] is provided in Fig. 6.

Regarding the mechanical properties of porous metals, not much literature exists. However, relating to nanoporous gold (NPG), being a relatively new research topic, the Young's modulus was determined by Huber et al. [26]. In this case, we got the numerical results from the authors. Since the data were given in GPa, we normalized them by $E = 81$ GPa, a value used in their reference. From all of the references, error bars were accurately transferred if available. If some of the used data do not have error bars, the errors are either not provided in the reference or the error bars are smaller than the symbol size in the diagram.

4. Comparison of experiments and model

4.1. Normalized fracture toughness

In Fig. 7, the experimental results for ceramics and polymers [2,8,9,11,18–22,24,25] are compared with the three model variants. It can be seen that the data for low porosities are near to model A (closed porosity), which makes sense. With increasing porosity, P, a transition takes place from variant A to B, and for porosities higher than 40% and ceramic materials, the variant C (open porosity with disconnections) yields the best agreement. This is what we would expect. Maiti et al. normalized their experimental data by dividing them through $\sigma_f\sqrt{(\pi w)}$ (Fig. 3 in Ref. [2]), which means that Eq. (1) becomes

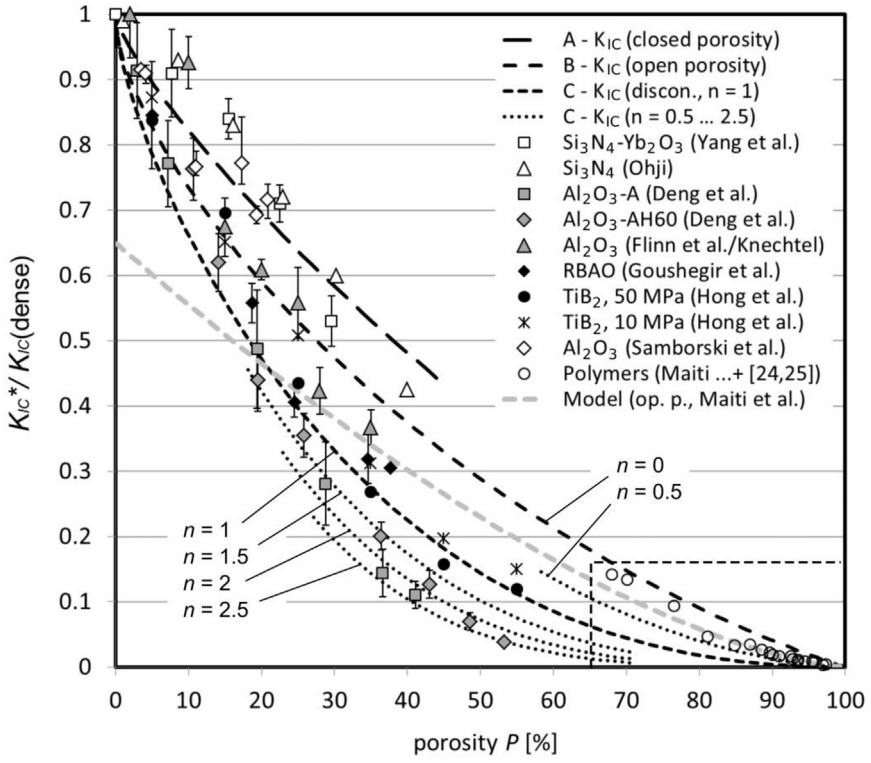

Fig. 7. Measured relative fracture toughness for different ceramic and polymer materials in comparison with the three variants of the geometric model (black dashed lines). Additionally, model C is provided with a set of curves for different exponents n. The materials with porosities below 60% are ceramics and above 60% polymers. The dashed grey line illustrates the model of Maiti et al. for open porosity [2]. All of the numerical, experimental data as well as some additional figures are provided in "Data in Brief" [23].

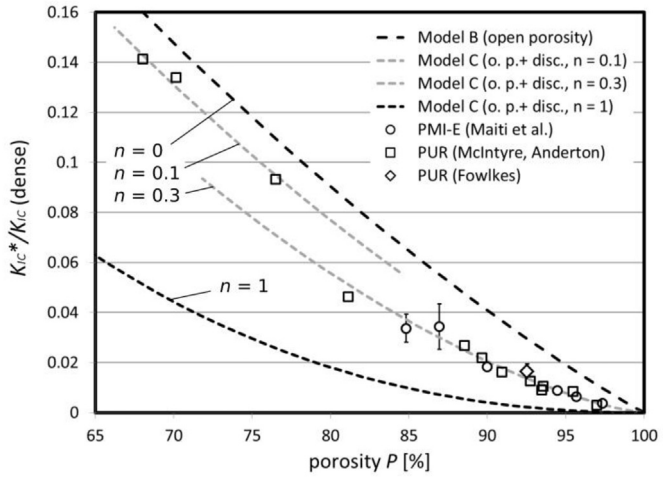

Fig. 8. Magnification of the small frame in Fig. 7, containing only the polymer data of Refs. [2,24,25].

$$\frac{K_{IC}^{*}}{\sigma_f\sqrt{\pi w}} = 0.65 \cdot \left(\frac{\rho}{\rho_s}\right)^{3/2} \tag{22}$$

This dependence is included as a grey dashed line in Fig. 7. Due to the normalization factor 0.65 [2], their model fits very well to the polymer data. However, the theoretical relative K_{IC} does not approach 1, if the porosity becomes zero. So, for low porosities the geometrical model, presented here, yields a better agreement with the experiment. Of course, Maiti et al. did not intend to describe low-porosity materials. If the experimental polymer data (open circles) are compared with our model, it can be seen that they are close to model B, in agreement with Maiti et al., who also used the "open porosity" variant of their model.

With $n = 1$, corresponding to the "basic" model C, 30% porosity – for example – means 30% disconnections, 50% porosity means 50% disconnections, etc. No disconnections means $n = 0$ (model B). In Fig. 7, we find that the low fracture toughness values from Deng et al. for porosities between 36% and 54% can be described quite well with exponents around $n = 2$ and 2.5, implying that the amount of disconnected beams is relatively large. In contrast, the

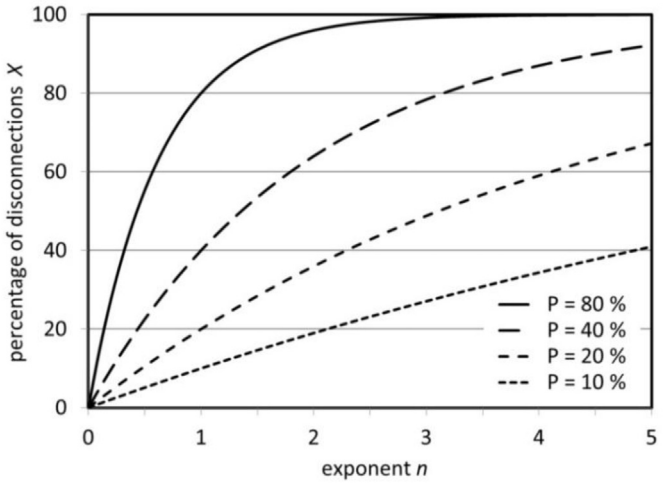

Fig. 9. The amount of disconnected ligaments as a function of the exponent n for different porosities P, according to Eq. (23).

high fracture toughness of silicon nitride at porosities below 30%, measured by Ohji [19] and Yang et al. [11], is even above the model predictions for closed porosity (model A). This is a hint that toughening mechanisms exist, which are not included in the model.

Fig. 8 represents a magnification of the small frame in the lower right corner of Fig. 7. Here, the polymer data got different labels according to their origins [2,24,25]. The data with porosities higher than 80% can be best fitted with $n = 0.3$. The reason for this low n-value at high porosities is that polymer materials tend to create thin beams and thin cell walls more easily than ceramics, because of their long molecular chains. Their amount of disconnections is much lower than that of ceramics.

The fact that these data are below the prediction of model B is again interpreted as missing ligaments and cell walls, respectively. Also Gibson/Ashby/Maiti had to lower their theoretical curve for open porosity (by the factor 0.65) to get agreement with the measurements.

4.2. Model C and the parameter n

To get an impression about the quantitative meaning of the exponent n in the equations of model C, some numbers are provided. The factor $(1 - P)^n$, e.g. in Eq. (21), describes the relative amount of *existing* ligaments in the porous material. The relative portion of disconnections X is given by

$$X = 1 - (1 - P)^n \tag{23}$$

Concerning the polymer data, the highest two data points in Fig. 8, for example, belong to ca. 70% porosity with $n = 0.1$. As per Eq. (23), this gives $X = 0.11$, meaning 11% disconnections, which is not much. The lowest fracture toughness of alumina (Deng et al. [18]) around 53% porosity with $n = 2.5$ (Fig. 7) yields 85% disconnections. Of course, the numbers of these examples should not be taken too seriously, but nevertheless, they provide an idea about the state of the microstructure. Based on the model, an overview of the dependence between disconnections, exponent n, and porosity P is provided in Fig. 9.

In ceramic materials, the transition from closed to open porosity is often expected at around 8%. This is supported by Yang et al., who determined separately the amounts of open and closed porosity in silicon nitride. Below 8% porosity they obtained closed porosity and above 15% open porosity. In between they measured a mixture of both states [11]. (Unfortunately, the other research groups, who tested ceramics, did not distinguish between different kinds of porosity.) In contrast, in Fig. 7 some measured fracture toughness values are still close to and even above the theoretical curve for closed porosity at porosities much higher than 8%. A possible explanation is that "isolated" pores are connected via very thin channels, e.g., along the triple conjunctions of the grains. But also the opposite behavior can be seen.

In Fig. 8, all of the polymer data with porosities above 65% are in the range of the "open porosity" variant, although at least PMI-E shows closed porosity. As already stated by Maiti et al. concerning man-made foams, the reason is probably that material from the cell walls is drawn to the cell edges by surface tension during the manufacturing process [2]. So, not only the type of porosity is essential but also the material distribution between the cells.

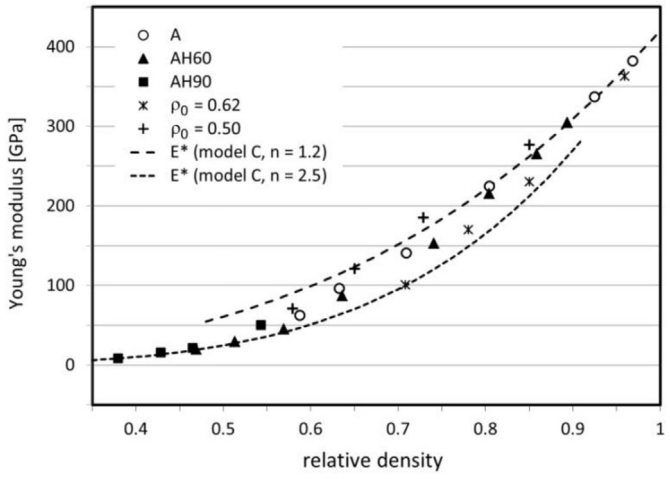

Fig. 10. Dependence of the Young's modulus on the relative density of porous Al_2O_3 ceramics prepared from different powders – see Fig. 4a) in the original paper of Deng et al. [18]. Here, Deng et al. included data from Lam et al. [27], who also tested porous alumina. Those materials were characterized by $\rho_0 = 0.62$ and $\rho_0 = 0.50$, representing the initial relative densities of the two types of Al_2O_3 compacts [18,27].

4.3. Normalized Young's modulus

4.3.1. Alumina

Comprehensive measurements of the elastic modulus with different alumina materials were provided by Deng et al. in Fig. 4a) of Ref. [18]. In order to be near to the original diagram, the absolute Young's modulus is plotted as a function of the relative density ρ/ρ_s. In this case, the theoretical curves of the model are multiplied by the (average) elastic modulus of the dense materials of 420 GPa, determined also by quadratic extrapolation. The comparison with model C in Fig. 10 shows that the main trend of the experimental data is well reproduced, in which the exponent n increases from approximately 1.2 at high densities to 2.5 at lower densities. This is again in accordance with the expectation that the number of disconnected ligaments increases with decreasing density.

It seems that for the same porosity the average lengths of the grains between the nodes, being rigid connections between the ligaments, can be different for different materials. This can be denoted by an average "aspect ratio" of the ligaments, even if the ligaments are not straight but curved. It seems that n characterizes an additional material property of porous materials, being independent of porosity and density of the parent material. So, in the case of entangled long grains (like a haystack) and with respect to the elastic modulus, the "ligament parameter" n yields additional information about the microstructure.

4.3.2. Nanoporous gold

The measured Young's moduli of NPG are displayed in Fig. 11 together with the model predictions of variant C. The experiments were not performed like usual, meaning that materials of different porosities were prepared and then tested individually. Instead, one kind of nanoporous gold was produced with a resulting porosity of $(74 \pm 1)\%$ and an average ligament diameter of (63 ± 6) nm (Huber et al. [26]). The used sample had cylindrical shape and was successively compressed, until the sample volume was reduced to half of the initial volume ($P = 37.7\%$). In between, the sample was unloaded completely, and the present Young's modulus was determined by means of the upper half of the unloading curves in the respective stress-strain diagram [26].

The steep initial increase of the Young's modulus, beginning at $P = 74\%$ in Fig. 11, was mentioned but not explained in the original paper. According to a subsequent paper, the anomalously high compliance can possibly be explained on an atomistic level by high local, surface-induced prestress on the ligaments, which already exists before loading the material [28].

At porosities between 71% and 73%, the data points reach a curve

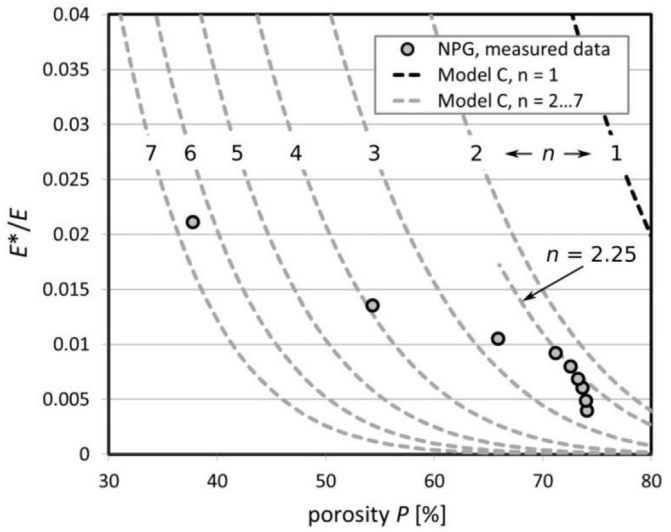

Fig. 11. Normalized Young's modulus of nanoporous gold (NPG) by analysis of the unloading/reloading cycles [26]. These values are in the range of model variant C with the "ligament parameter" n between 2 and 7.

of model C with the minimum value $n = 2.25$, meaning that from the beginning a lot of disconnected ligaments exist. This agrees very well with [17], where the anomalously low stiffness of nanoporous gold was explained by broken and dangling ligaments. During further compression of the same sample, E^* increases only slightly and on a much lower rate than the model-C curves. Consequently, the parameter n rises up to 6.5, which implies that the number of disconnected ligaments also strongly increases. This behavior can be understood, because when compressing a filigree network of thin metallic ligaments down to a volume of 50%, the structure naturally crushes successively. Additionally, bending effects reduce the Young's modulus (See also tests and simulation in Ref. [28].). This is supported as well by stress-strain curves, given in Ref. [26], where the overall dissipated energy due to inelastic processes is about one to two orders of magnitude larger than the energy, created by one cycle of elastic loading. (This follows from considering corresponding areas under the stress-strain curves.)

4.4. Some remarks

In a paper of Ziehmer et al. [29], the microstructure of NPG was characterized by two parameters κ_1 and κ_2, being the two average principal curvatures (inverse radii) on the surface of a ligament. The first one is measured perpendicular and the second one parallel to the alignment of the ligament. Nevertheless, they found that both parameters are roughly correlated so that the microstructure can be described by a single parameter. In a related paper of Hu et al. [30], a quantity like "scaled connectivity density" within the framework of both morphology and topology was used to determine the microstructure. So, other approaches and parameters exist to describe the structure in case of nanoporous gold. However, we will not further examine whether a relation to our parameter n exists, because with NPG we would only treat a special case, and it would exceed the scope of this paper.

Generally, it is impossible to describe all of the experimental fracture toughness data by a single theoretical function (see Fig. 7). Different materials follow different paths in the diagram, which can be best explained by different kinds of porosity and microstructure. For one material, it seems that it is not the only way to reproduce $K_{IC}(P)$ by a single (phenomenological) function, particularly, if the topological properties of the microstructure change with increasing porosity. In the given model, the experimental data are not evaluated by fitting one theoretical curve to the measurement. Instead, the measured data are plotted together with the family of curves (reference curves) corresponding to the different model variants, and thus, some information about the microscopic structure of the porous material and its individual kind of porosity can be obtained.

An important question applies to the scale independence of the given model. In principle, two effects can cause a dependence on the pore size. A surface effect, like material segregation on the pore's surface, can influence quantities like, e.g., the surface energy, hardness, or strength in the surface region. So, if using the same parent material and decreasing the pore size by leaving the porosity constant, the total surface area increases drastically, and this can influence the fracture toughness. The second reason is an effect, caused by the size of the "notch root radius." It means that a crack would grow more easily through small pores than through large pores. However, this effect is valid basically for 2D-structures like, e.g., a material with cylindrical "pores," extending through the whole sample. Let's assume that a crack passes through such a hollow cylinder with the crack face being parallel and the propagation direction being perpendicular to the longitudinal axis of the cylinder. Then a large radius of the cylinder acts like crack tip blunting and impedes crack propagation more than a small radius. However, in the three-dimensional case of spherical pores, this effect is much less pronounced, because the amount of crack front hitting a curved surface is considerably less. Due to a lack of corresponding experimental data, a potential independence (or dependence) of the fracture toughness on the pores size, at constant porosity, is a good objective for future research.

If the material characteristics show deviations regarding isotropy, homogeneity of pore distribution, linearity, compactness of pore shapes, etc., these aspects have to be considered if applying the model. A modification of our model ansatz by a more realistic approach, concerning shapes as well as spatial and size distribution of the pores, would possibly cause some improvement. Nevertheless, we assume that this would lead only to minor changes of the predicted results. Moreover, the model would probably become less general and more complicated. The present model has the advantage that it can be applied easily due to a full set of analytical equations and that it can be used for a wide range of experiments and materials. At least, it should be of some help for the mechanical characterization of porous materials.

5. Conclusions

A simple 3D geometrical model is presented, which describes the relative toughness, fracture toughness, and Young's modulus of porous materials by analytical functions of the porosity. It is based on the cubic structure and consists of three different variants, being "closed porosity" (A), "open porosity" (B), and "open porosity with disconnections" (C). The model assumes that the toughness is proportional to the relative amount of substantial crack surface and that fracture occurs along the path with the minimum area of substantial crack face. It can be applied for any porosity between 0 and 1. A dependence on the cell size does not exist. The three variants are in good agreement with a large amount of experimental data. With increasing porosity in ceramic materials, the transition from closed to open porosity is reflected well by a change from model A to B and then to C. Instead of a variety of different descriptions in the literature, these variants yield three fundamental curves, which are independent of any arbitrary parameter and independent of material properties, except the porosity itself and the fracture toughness of the dense material. Only model C has a variable parameter that yields quantitative information about the

amount of disconnected ligaments or the aspect ratio of the remaining ligaments.

Acknowledgement

Concerning the program Maple, we are indebted to get some help from Henry E. Mgbemere and Diego Blaese. We thank also Ayse Kalemtas for providing relevant literature, Jürgen Markmann for helpful information and sending us numerical experimental data concerning nanoporous gold, as well as Hai-Jun Jin for the permission to use a figure (Fig. 5) from one of his publications. The authors gratefully acknowledge financial support from the German Research Foundation (DFG) via SFB 986 “M3”, project A6.

Appendix A. Derivation of Eq. (11)

Equation (10) presents the solution of $P = 2d^3 - 3d^2 + 1$ (Eq. (8)). For an easier reading, this solution – calculated with *Maple* – is given once more (So, Eqs. (A1) and (10) are identical.).

$$d = \frac{1}{2}\cdot\left(-1+2P+2\sqrt{P^2-P}\right)^{1/3} + \frac{1}{2\left(-1+2P+2\sqrt{P^2-P}\right)^{1/3}} + \frac{1}{2} \tag{A1}$$

As already said, the term under the square root is negative (except for $P = 0$), and therefore, both expressions in brackets are complex. Concerning the third root, note that any number – except zero – has three different complex cubic roots, and the square root inside the brackets has two different solutions, namely “+” and “−“. This yields six different combinations for each bracket term in Eq. (A1) and together, in principle, 36 possible combinations. Not every combination and especially not every third root yields the solution we need. Apart from that, a computer normally calculates in the “real mode” and gives an error message if trying to extract the root of a negative number. What we would like to have is the normalized toughness as a simple real function of P. With the assumption that P is non-negative and smaller than 1, we can write Eq. (A1) in the complex notation with $\sqrt{(P-P^2)}$ being real:

$$d = \frac{1}{2}\cdot\left(2P-1+\ i\cdot 2\sqrt{P-P^2}\right)^{1/3} + \ \frac{1}{2}\cdot\left(2P-1-\ i\cdot 2\sqrt{P-P^2}\right)^{1/3} + \frac{1}{2} \tag{A2}$$

The bracket in the denominator of the second term in Eq. (A1) vanishes, because the absolute value of the complex number in each bracket is 1. (The reader might verify this easily.) This allows for replacing the real and the imaginary part in both brackets of the equation (A2) by trigonometric functions as follows: $2P-1 = \cos\ \alpha$ and $2\sqrt{(P-P^2)} = \sin\ \alpha$. According to $\cos\ \alpha + i\ \sin\ \alpha = e^{i\alpha}$ and $\alpha = \cos^{-1}(2P-1)$, Eq. (A2) becomes

$$d = \frac{1}{2}\cdot\left(e^{i\ \cos^{-1}(2P-1)}\right)^{1/3} + \ \frac{1}{2}\cdot\left(e^{-i\ \cos^{-1}(2P-1)}\right)^{1/3} + \frac{1}{2} \tag{A3}$$

If we now multiply the exponents in the brackets by 1/3, we get only one solution out of three, and – apart from that – the solution is not that one we are looking for. We obtain the other two solutions by replacing $\cos^{-1}(2P-1)$ in both imaginary exponents by $\cos^{-1}(2P-1) \pm 2\pi$. This does not change the exponential terms themselves but their cubic roots. In principle, we can treat these two exponents differently, like adding 2π in the first bracket and leaving the second bracket unchanged. However, in most cases d wouldn't be real anymore. If we treat both exponents in the same way and apply $\cos\ \alpha = (e^{i\alpha} + e^{-i\alpha})/2$, we get

$$d = \cos\left(\frac{\cos^{-1}(2P-1)+2\pi k}{3}\right) + \frac{1}{2} \tag{A4}$$

with k being −1, 0, or 1. For $k = 0$, the ratio d would become larger than 1, and for $k = 1$, the relative toughness G_C^*/G_C for $P = 0$ would be 0.25 with a negative d. Both cases do not describe the physical situation. The desired solution means $k = -1$. So, by inserting the corresponding d from Eq. (A4) into Eq. (9), we obtain directly the target equation (11) for open porosity (variant B).

Appendix B. Calculation of normalized Young's moduli

For a parallel arrangement of two materials (constant strain), the general relation for the combined Young's modulus is

$$E(\text{par.}) = fE_1 + (1-f)E_2 \tag{B1}$$

with E_1 and E_2 being the elastic moduli of the involved materials and f being the normalized volume fraction of the first material (E_1). The Young's modulus of a serial arrangement (constant stress) is given by

$$E(\text{ser.}) = \left(\frac{f}{E_1} + \frac{1-f}{E_2}\right)^{-1} \tag{B2}$$

Applying these rules, we start with closed porosity. First, we calculate the combined elasticity of the horizontal layer of thickness $w-t$ (Fig. 1) in a parallel arrangement of solid material and pores. With E being the elastic modulus of the solid material and again $d = t/w$, we get for the layer, containing the pores, the elastic modulus E_1:

$$E_1 = \frac{t^2(w-t)+2t(w-t)^2}{w^2(w-t)}\cdot E + \frac{(w-t)^3}{w^2(w-t)}\cdot 0 = \left(-d^2+2d\right)\cdot E \tag{B3}$$

Secondly, we determine the combined elasticity of this layer plus the underlying solid layer of thickness t in a serial arrangement. However, the latter layer cannot be treated that simply, because the layer is not totally under homogeneous stress, depending on the porosity. The respective volumes are illustrated in Fig. B.1.

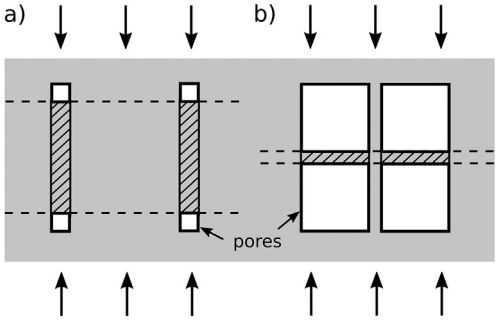

Fig. B.1. a) Low porosity and b) high porosity. The shaded solid areas between the pores contribute differently to the overall elastic modulus. The arrows indicate the mechanical loading situation. The layers (of thickness t) between the dashed lines contain only solid material.

In case of very low porosity (Fig. B.1a), it becomes clear that the shaded volumes between the pores act under compression as solid material. In case, the porosity approaches 1, like in Fig. B.1b, the corresponding shaded volumes do not contribute at all under compression. So, in the following calculation we supply the shaded volume with an “efficiency factor” d^m, where m is of the order of 1.

For low porosity, d^m is almost 1 and for high porosity d^m is close to 0. Further down, it will be shown that a variation of the exponent m does not have much influence on the final result.

With respect to Fig. 1, we get for the horizontal solid layer between the pores the following Young's modulus E_2:

$$E_2 = \frac{t^3 + 2t^2(w-t)}{w^2 t}\cdot E + \frac{t(w-t)^2}{w^2 t}\cdot d^m \cdot E = \left[-d^2 + 2d + (1-d)^2 d^m \right]\cdot E \tag{B4}$$

The two layers of Eqs. (B3) and (B4) have relative volume fractions of $1-d$ and d, respectively. So, combining the two layers in a serial arrangement yields the following elastic modulus E^* for the material of closed porosity (variant A) with $d = 1 - P^{1/3}$ (Eq. (5)):

$$E^* = \left(\frac{1-d}{E_1} + \frac{d}{E_2} \right)^{-1} \tag{B5}$$

$$\Rightarrow \frac{E^*}{E}(\text{mod. A}) = \left(\frac{1-d}{-d^2+2d} + \frac{1}{-d+2+(1-d)^2 d^{m-1}} \right)^{-1} \tag{B6}$$

For open porosity, we refer to Fig. 2 and calculate E^*/E in an analog way. Again, we start with the horizontal layer of thickness $w-t$. The combined Young's modulus of this layer is

$$E_1 = \frac{t^2(w-t)}{w^2(w-t)}\cdot E = d^2 \cdot E \tag{B7}$$

For the other layer of thickness t, we get by considering the factor d^m:

$$E_2 = \left(\frac{t^3}{w^2 t} + \frac{2t^2(w-t)}{w^2 t}\cdot d^m \right)\cdot E = \left[d^2 + 2(1-d)\cdot d^{m+1} \right]\cdot E \tag{B8}$$

The serial arrangement of both layers for open porosity (variant B) yields:

$$\frac{E^*}{E}(\text{mod. B}) = \left(\frac{1-d}{d^2} + \frac{1}{d + 2(1-d)\cdot d^m} \right)^{-1} \tag{B9}$$

Concerning the model variant C, we also have to adapt the elastic modulus. If the ligaments vanish in proportion to $(1-P)^n$, as in Eq. (13), they cease to contribute to the elastic modulus. Therefore, the Young's modulus, corresponding to Eq. (B7) of variant B, would also get an additional factor $(1-P)^n$. In Eq. (B8), two summands exist in the square brackets. The second summand corresponds to the ligaments and clearly gets the same factor. The first summand stands for the junction of the ligaments (nodes) with the volume t^3 (Fig. 2). But even if these volumes do not vanish, they do not contribute to the elastic modulus like before, if one or more adjacent ligaments are disconnected. It follows that the final relative Young's modulus in Eq. (B9) just gets the mentioned factor, and we obtain for model variant C:

$$\frac{E^*}{E}(\text{mod. C}) = \left(\frac{1-d}{d^2} + \frac{1}{d + 2(1-d)\cdot d^m} \right)^{-1} \cdot (1-P)^n \tag{B10}$$

In order to obtain E^*/E in Eqs. (B9) and (B10) as a function of P, d has to be replaced by Eq. (17).

Next, we have to determine the exponent m for the models A to C. We begin with variant B. If the wall thickness t and the "inner" size of the pores $w-t$ are equal, which means $d = 0.5$, the corresponding shaded volume (compare with Fig. B.1) is cubical-shaped. Because it has contact on two side faces, which creates an inhomogeneous stress field in the shaded volume, we assume that the volume participates approximately with 50% compared to the case of homogeneous, full compression. This means that we have $m = 1$, because then $d^m = 0.5$. This m-value is used also for model C.

In the case of closed porosity (variant A), the shaded volume in Fig. B.1 has contact on each of the four side faces. So, the influence becomes stronger. Therefore, we estimate $m = 0.5$, which yields a factor of $0.5^{0.5} \approx 0.71$, correspondingly. These two choices, of course, include some uncertainty, but we think that the two exponents describe quite well the influence of the shaded volumes on the elastic modulus.

Moreover, the influence of m on the final result K_{IC}^*/K_{IC} is weak, as can be seen in Fig. B.2. For each variant A–C, the curves are given for the exponents $m = 0.5$, 1, and 1.5. But although the influence is low, the most reasonable values have been chosen. As already said, we fix them to $m = 0.5$ for model A and to $m = 1$ for the models B and C. By inserting these m-values into Eqs. (B6), (B9), and (B10), we finally get the normalized Young's moduli in Eqs. (14)–(16).

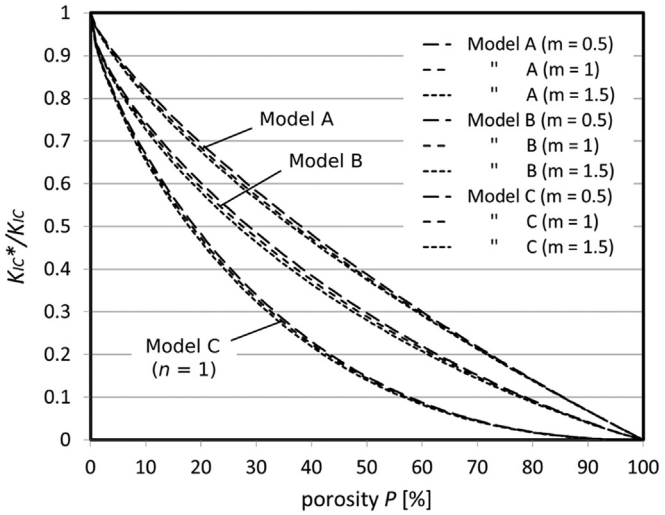

Fig. B.2. Normalized fracture toughness for the models A, B, and C with three different parameters m for each model variant.

References

[1] S.K. Ashby, The mechanical properties of cellular solids, the Metallurgical Society of AIME, Metallurgical Transactions A 14A (1983) 1755–1769.
[2] S.K. Maiti, M.F. Ashby, L.J. Gibson, Fracture toughness of brittle cellular solids, Scripta Metall. 18 (1984) 213–217.
[3] L.J. Gibson, M.F. Ashby, Cellular Solids, Structure and Properties – Second Ed, University Press, Cambridge, 1999.
[4] R. Brezny, D.J. Green, C. Quang Dam, Evaluation of strut strength in open-cell ceramics, J. Am. Ceram. Soc. 72 (6) (1989) 885–889.
[5] J. Zeschky, F. Goetz-Neunhoeffer, J. Neubauer, S.H. Jason Lo, B. Kummer, M. Scheffler, P. Greil, Preceramic polymer derived cellular ceramics, Compos. Sci. Technol. 63 (2003) 2361–2370.
[6] S.-R. Wang, H.-R. Geng, L.-H. Hui, Y.-Z. Wang, Reticulated porous multiphase ceramics with improved compressive strength and fracture toughness, JMEPEG 16 (2007) 113–118.
[7] A.S. Wagh, J.P. Singh, R.B. Poeppel, Dependence of ceramic fracture properties on porosity, J. Mater. Science 28 (1993) 3589–3593.
[8] B.D. Flinn, R.K. Bordia, A. Zimmermann, J. Rödel, Evolution of defect size and strength of porous alumina during sintering, J. Europ. Ceram. Soc. 20 (2000) 2561–2568.
[9] M. Knechtel, Präparation und Charakterisierung metallverstärkter Keramiken mit interpenetrierenden Netzwerken, Dissertation, Technische Universität Hamburg-Harburg, Hamburg, 1996.
[10] E. Linul, L. Marsavina, Prediction of fracture toughness for open cell polyurethane foams by finite-element micromechanical analysis, Iran. Polym. J. (Engl. Ed.) 20 (9) (2011) 735–746.
[11] J.-F. Yang, T. Ohji, S. Kanzaki, A. Diaz, S. Hampshire, Microstructure and mechanical properties of silicon nitride ceramics with controlled porosity, J. Am. Ceram. Soc. 85 (6) (2002) 1512–1516.
[12] P. Thiyagasundaram, J. Wang, B.V. Sankar, N.K. Arakere, Fracture toughness of

foams with tetrakaidecahedral unit cells using finite element based micromechanics, Eng. Fract. Mech. 78 (2011) 1277–1288.
[13] R.W. Rice, Porosity of Ceramics, Marcel Dekker, Inc, New York, Basel, Hong Kong, 1998. ISBN 0.8247-0151-8 168 ff.
[14] M. Scheffler, P. Colombo (Eds.), Cellular Ceramics, Wiley-VCH-Verlag, Weinheim, 2005.
[15] M.F. Ashby, Y.J.M. Bréchet, Designing hybrid materials, Acta Mater. 51 (2003) 5801–5821.
[16] Maple 18, A Computer Algebra System and Numeric Computation, Developer: Maplesoft, Waterloo Maple Inc, Waterloo (Ontario), Canada, 2014.
[17] L.-Z. Liu, X.-L. Ye, H.-J. Jin, Interpreting anomalous low-strength and low-stiffness of nanoporous gold: quantification of Network Connectivity, Acta Mater. 118 (2016) 77–87.
[18] Z.-Y. Deng, T. Fukasawa, M. Ando, G.-J. Zhang, T. Ohji, Microstructure and mechanical properties of porous alumina ceramics fabricated by the decomposition of aluminum hydroxide, J. Am. Ceram. Soc. 84 (11) (2001) 2638–2644.
[19] T. Ohji, Microstructural design and mechanical properties of porous silicon nitride ceramics, Mater. Sci. Eng. 498 (2008) 5–11.
[20] C. Hong, X. Zhang, J. Han, B. Wang, Fabrication and mechanical properties of porous TiB_2 ceramic, J. Mater. Sci. 41 (2006) 4790–4794.
[21] S. Samborski, T. Sadowski, Dynamic fracture toughness of porous ceramics, J. Am. Ceram. Soc. 93 (11) (2010) 3607–3609.
[22] S.M. Goushegir, P.O. Guglielmi, J.G.P. da Silva, M.P. Hablitzel, D. Hotza, H.A. Al-Qureshi, R. Janssen, Fiber-matrix compatibility in an all-oxide ceramic composite with RBAO matrix, J. Am. Ceram. Soc. (2011) 1–6.
[23] H. Jelitto, G. A. Schneider, Fracture toughness of porous materials – a compilation of experimental methods and data. Data in Brief (submitted).
[24] A. McIntyre, G.E. Anderton, Fracture properties of a rigid polyurethane foam over a range of densities, Polymer 20 (2) (1979) 247–253.
[25] C.W. Fowlkes, Fracture toughness tests of a rigid polyurethane foam, Int. J. Fracture 10 (1) (1974) 99–108.
[26] N. Huber, R.N. Viswanath, N. Mameka, J. Markmann, J. Weißmüller, Scaling laws of nanoporous metals under uniaxial compression, Acta Mater. 67 (2014) 252–265.
[27] D.C.C. Lam, F.F. Lange, A.G. Evans, Mechanical properties of partially dense alumina produced from powder compacts, J. Am. Ceram. Soc. 77 (8) (1994) 2113–2117.
[28] B.-N.D. Ngo, A. Stukowski, N. Mameka, J. Markmann, K. Albe, J. Weissmüller, Anomalous compliance and early yielding of nanoporous gold, Acta Mater. 93 (2015) 144–155.
[29] M. Ziehmer, K. Hu, K. Wang, E.T. Lilleodden, A principle curvature analysis of the isothermal evolution of nanoporous gold: quantifying the characteristic length-scales, Acta Mater. 120 (2016) 24–31.
[30] K. Hu, M. Ziehmer, K. Wang, E.T. Lilleodden, Nanoporous gold: 3D structural analyses of representative volumes and their implications on scaling relations of mechanical behaviour, Phil. Mag. 96 (32–34) (2016) 3322–3335.